Numerical analysis of a negative emission technology of methane to mitigate climate change

Numerical analysis of a negative emission technology of methane to mitigate climate change

Hanbing Xiong[1], Tingzhen Ming[1, *], Yongjia Wu[1], Wei Li[3], Liwen Mu[4], Renaud de Richter[5], Suying yan[6], Yanping Yuan[7], Chong Peng[2]

1. School of Civil Engineering and Architecture, Wuhan University of Technology, Wuhan 430070, China

2. School of Urban Planning and Architecture, Huazhong University of Science and Technology, Wuhan 430074, China

3. Institute for Materials and Processes, School of Engineering, The University of Edinburgh, Edinburgh EH9 3FB, Scotland, UK

4. College of Chemical Engineering, State Key Laboratory of Materials-oriented Chemical Engineering, Nanjing Tech University, Nanjing, 211816, PR China

5. Tour-Solaire.Fr, 8 Impasse des Papillons, F34090 Montpellier, France

6. College of Energy and Power Engineering, Inner Mongolia University of Technology, Hohhot 010051, China

7. School of Mechanical Engineering, Southwest Jiaotong University, Chengdu 610031, China

Corresponding Author:

Tingzhen Ming: School of Civil Engineering and Architecture, Wuhan University of Technology, Wuhan 430070, China. Email: tzming@whut.edu.cn

Abstract: The increase of 1.09°C in global temperature resulted in significant catastrophes because of the extreme climate. The climate change rate can be slowed down by reducing the levels of CH_4 and CO_2 in the atmosphere. The solar chimney power plant integrated with a honeycomb photocatalytic reactor (SCPP-HPCR) uses the photocatalytic technology to remove atmospheric CH_4. In addition, CO_2 emissions can be reduced from coal fired power plant due to the generating capacity of the system. In this paper, the influence of the geometric parameters of the reactor on the turbine efficiency and overall performance of the SCPP-HPCR are studied by numerical simulation. The obtained results showed that the flow resistance inside the system was

mostly caused by the HPCR at low turbine speed, and primarily by the turbine at high turbine speed. Reducing the pore diameter of the reactor could improve the photocatalytic performance of the SCPP-HPCR more than increasing the turbine speed. The SCPP-HPCR having a pore diameter of 3 mm, porosity of 0.85, and constant turbine speed of 180 rpm, built in Qianyanzhou, China, could remove 2.38 kg of CH_4 and reduce 375.52 kg of CO_2 in one day.

Keywords: Solar chimney; Remove CH_4; Reduce CO_2 emissions; Climate change, Numerical simulation.

Nomenclature

B, B_1, B_2	Constants for reaction rate calculation
$C_{1\varepsilon}$, $C_{2\varepsilon}$	Constants for turbulent model
c_1	CH_4 concentration, $mol \cdot m^{-3}$
c_2	O_2 concentration, $mol \cdot m^{-3}$
r_m	Reaction rate of CH_4, $mol \cdot W^{-1} \cdot m^{-1} \cdot s^{-1}$
G	Solar radiation, $W \cdot m^{-2}$
q	Heat flux of ground, $W \cdot m^{-2}$
SSA	Specific surface area, m^{-1}
$\vec{J_i}$	Diffusion flux of species i, $mol \cdot s^{-1} \cdot m^{-3}$
Q_m	Mass flow rate, $kg \cdot s^{-1}$
m_1	Mass fraction of CH_4 at the entrance
m_2	Mass fraction of CH_4 at the exit
P_t	Output power of the system, kW
S_Φ	Momentum loss term, $N \cdot m^{-3}$
S_i	Additional rate owing to the discrete phase, $kg \cdot m^{-3} \cdot s^{-1}$
$\dot{m}1_{CO_2}$	Reduction rate of CO_2 emission from the coal-fired power station, $kg \cdot h^{-1}$
$\dot{m}2_{CO_2}$	Reduction rate of CO_2 equivalent from photocatalytic CH_4, $kg \cdot h^{-1}$
$\dot{C_{eq}}$	CO_2 reduction rate, $kg \cdot h^{-1}$
Greek symbols	
v	Kinetic viscosity, $m^2 \cdot s^{-1}$
β	Coefficient of thermal expansion, K^{-1}
ρ	Gas density, $kg \cdot m^{-3}$
τ	Shear stress, $N \cdot m^{-2}$
k	Karman Constant

Abbreviations	
GWP	Global warming potential
SCPP	Solar chimney power plant
HPCR	Honeycomb photocatalytic reactor
IPCC	Intergovernmental panel on climate change

1. Introduction

The global climate change caused by the increasing global temperature was a significant challenge for this century. The maximal temperature increase that the Earth could withstand should be limited to 2 °C when compared with the pre-industrial periods, and it should not exceed 0.1 °C each decade (Vellinga and Swart, 1991). According to the Intergovernmental Panel on Climate Change (IPCC) (Masson-Delmotte et al., 2021), the global average temperature in 2020 was 1.09 °C warmer than that in the 20th century, with an increase of 1.59 °C on land and 0.88 °C in ocean. Extreme events caused by climate anomalies, such as localized droughts or heavy rainfall, forest fires, and biological extinctions, were frequently occurred (Wang et al., 2022). In addition, other terrifying events prompted by global warming had the potential to bring great danger to people in the future, such as the loss of seasonal snowpack, glacier melting, permafrost thawing, and decrease in summer Arctic sea ice (Witze, 2019). To achieve the Paris Agreement's target of restricting global warming to 1.5°C, the greenhouse gas emissions should be promptly and significantly decreased.

It was widely believed that removing CO_2 from the atmosphere could significantly mitigate climate change. Many active greenhouse gas mitigation technologies, such as carbon capture, utilization, and storage (CCS) (Bui et al., 2018), bioenergy with carbon capture and storage (BECCS) (Sanchez et al., 2018), and direct air capture (DAC) (House et al., 2011) were proposed. CH_4 owns a global warming potential (GWP) 84 times higher than CO_2. Although the concentration of CH_4 in the atmosphere was low, it had a contribution of 16 % of the global warming impact. The greenhouse effect caused by CH_4 had attracted global attention as the atmospheric CH_4 concentration was increasing from pre-industrial of 0.76 ppm to 1.8 ppm today, with an increasing rate much higher than that of CO_2. Almost 40 % of CH_4 emission was from natural sources,

such as wetlands and termites. In addition, other 60% were from anthropogenic, such as ruminants, rice agriculture, fossil fuel extraction, landfills, and biomass burning (Allen, 2016). The atmospheric persistence of CH_4 was short, and therefore reducing the emissions could achieve a substantial climate mitigation effect in a short time frame (Kuylenstierna et al., 2021). Moreover, 90 % of the atmospheric CH_4 was oxidized by hydroxyl radicals, which promoted the ozone production and affected the oxidation performance of the tropospheric (Galpern, 2021). Furthermore, high ozone levels could endanger human health, affect plant and animal growth, and cause photochemical haze.

The existing methods for atmospheric CH_4 removal include zeolites, soil amendments, iron salt aerosols, biofilters, and photocatalysts. Forest soils were considered as significant CH_4 sink, neutralizing 13 % of anthropogenic carbon emissions (Price et al., 2004). However, developing effective CH_4 removal methods was crucial due to the fact that it could take too long for ecosystems to naturally decompose the atmospheric CH_4. Brenneis et al. (Brenneis et al., 2021) synthesized a Cu-dropped zeolite as a thermocatalyst, which removed 100 % of CH_4 at atmospheric levels, at a reaction temperature of 310 °C. Although this catalyst could sustain high activity after 300 h of recycling, the high temperature environment required for the reactions restricted the large-scale development of this technology. Iron-salt aerosols could remove atmospheric CH_4 by increasing the level of Cl^- in the air. However, more studies should be conducted to evaluate the feasibility of this technology (Ming et al., 2021a). Moreover, some new removal methods were being investigated (Wang et al.). CH_4 could be converted to less potent greenhouse gas CO_2 under sunlight at room temperature and pressure, using the photocatalytic semiconductor technology (de Richter et al., 2017).

The solar chimney power plant (SCPP), which is a green thermal wind power generating system, can develop a steady upward airflow inside the chimney. However, it had a low overall effectiveness (Vazquez-Ruiz et al., 2022). Many researchers tried to improve the solar energy utilization efficiency of the SCPP, or used it for other objectives, such as the desalination of saltwater (Zuo et al., 2020) and the drying of food (Maia and Silva, 2022). Some economic evaluation and internal optimization

methods had also been extensively studied (Zuo et al., 2021; Zuo et al., 2022). The SCPP also performed well in terms of cleaning urban air. It produced a stable airflow with physical filtering to purify the particulates in the city air (Cao et al., 2015). Cao et al. (Cao et al., 2018) designed and constructed the first haze removal tower in Xi'an, China, with a collector size of 43 m × 60 m and a chimney height of 60 m, which confirmed the viability of improving urban air quality with the SCPP from an engineering standpoint.

The IPCC highlighted de Richter's proposal (de Richter et al., 2017) of combining the SCPP with photocatalysis as a practicable strategy for removing CH_4 on a large scale (Fuss et al., 2018; Minx et al., 2018). The types of reactors and the photocatalytic were the critical factors affecting the photocatalytic performance of the system. The honeycomb photocatalytic reactor (HPCR) having a large specific surface area is an efficient photocatalytic reactor. In addition, the internal flow field was rectified by placing the HPCR within the collector (Zhang et al., 2022). Many laboratory tested for CH_4 between 50 ppm and 1000 ppm demonstrated that its conversion rate and product selectivity were significantly improved by the addition of noble metals to the TiO_2 (Ahmed et al., 2022; Li, Y. et al., 2019; Li, Z. et al., 2019; Sekar et al., 2021). It was important to mention that Ag/ZnO, which was a novel photocatalyst, could be activated by sunlight and it can convert CH_4, with a concentration of 50 ppm, to CO_2 in 20 min. The catalytic efficiency was even better with lower concentration (Chen et al., 2016). Ming et al. (Ming et al., 2021b) conducted numerical simulations to first study the factors affecting the performance of the SCPP-HPCR without considering the power generation. The output power of the system can be reliably estimated by converting the 3-D turbine to the surface of pressure drop (Pastohr et al., 2004). However, the real fluid trace inside the system could not be simulated. Guo et al. (Guo et al., 2014) more precisely evaluated the performance of the SCPP by considering both the 3-D turbine and the solar radiation model. For the SCPP-HPCR, the main performances of the system are the degradation of atmospheric CH_4 by the reactor and the turbine power generation. Both could affect the flow of air in the SCPP-HPCR, and knowing the relationship between them can significantly improve the system performance.

In this paper, a numerical model is first developed to study the overall performance of the SCPP-HPCR considering 3-D turbine. The parameters of the reactor including the pore diameter, porosity, and operating conditions of the turbine are optimized. This provides a reference for the future design and construction of the SCPP-HPCR. Furthermore, taking into account the CH_4 removal and renewable electricity generation, the equivalent CO_2 emission reduction of the SCPP-HPCR is discussed.

2. Computation model

2.1 Geometric model

The dimension of the geometric model match that of the Spanish prototype (Haaf, W, 1984). The radius of the collector is 120 m, and its height linearly varies from 2 m at the entrance to 6 m at the bottom of the chimney. The chimney has a radius of 5 m and a height of 200 m. The CLARK-Y airfoil is used in the axial turbine, which is located at the bottom of the chimney at a height of 7 m above the ground (Tingzhen et al., 2008), as shown in Fig. 1.

The starting of the HPCR is at 10 m from the entrance inside the canopy. The reactor is made of perspex with good light transmission. The P25 photocatalyst is uniformly distributed on the inner wall of the honeycomb channel. Note that P25 is selected due to the fact that it is cheap and stable, and it has a good film formation property (Ma and Yang, 2010). It is more efficient to remove CH_4 by increasing the reactor length. However, the HPCR length is kept at 5 m in this study, because a longer reactor can diminish the ability of the ground to absorb solar energy.

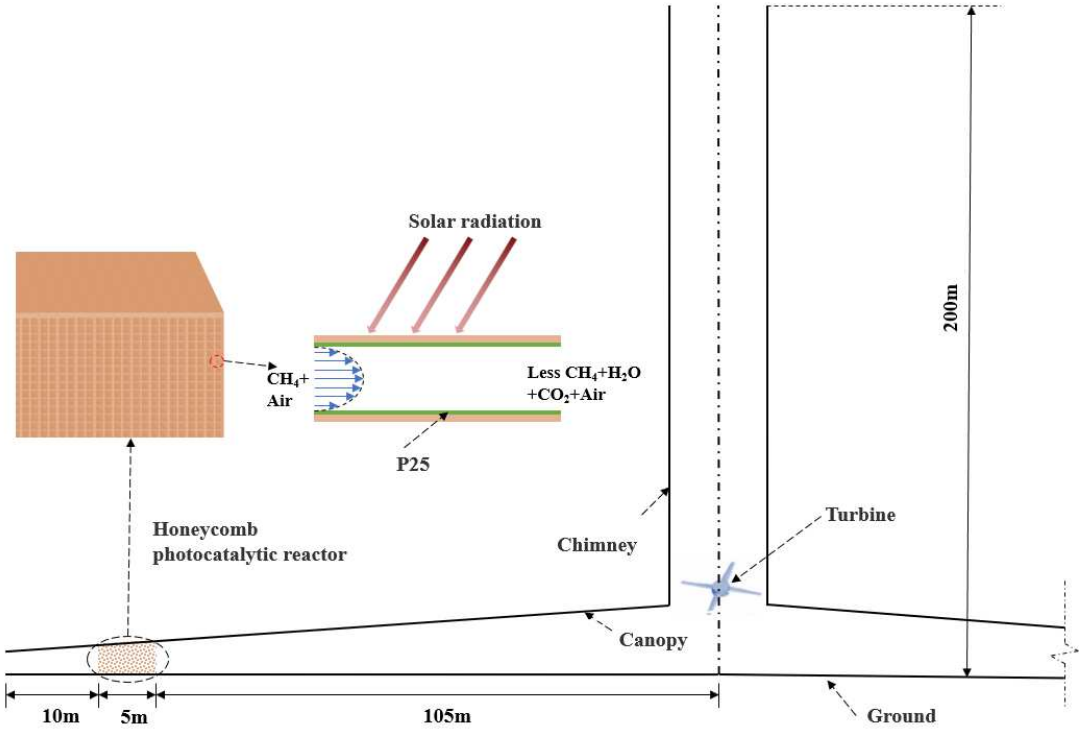

Fig. 1. Schematics of the geometrical model.

2.2 Numerical model

The Rayleigh number ($R_a = \frac{g\beta\Delta T H^3}{av}$) is a dimensionless number associated with buoyancy-driven convection. The flow in the SCPP-HPCR is fully turbulent due to $R_a \geq 10^{10}$ (Tingzhen et al., 2006). The governing equations, including the continuity, momentum, energy, RNG *k*-*ε*, and transport equations, are expressed as:

Continuity equation

$$\frac{\partial(\rho u_i)}{\partial x_i} = 0 \tag{1}$$

Momentum equation

$$\frac{\partial(\rho u_i u_j)}{\partial x} = \rho g - \frac{\partial p}{\partial x_i} + \frac{\partial \tau_{ij}}{\partial x_j} \tag{2}$$

Energy equation

$$\frac{\partial(\rho c_p u_j T)}{\partial x_j} = \frac{\partial}{\partial x_j}\left(\lambda \frac{\partial T}{\partial x_j}\right) - \tau_{ij}\frac{\partial u_i}{\partial x_j} + \beta T\left(\frac{\partial p}{\partial x_j} + u_j \frac{\partial p}{\partial x_j}\right) \tag{3}$$

Equation for the turbulent kinetic energy (k)

$$\frac{\partial}{\partial x_i}(\rho k u_i) = \frac{\partial}{\partial x_j}(\alpha_k \mu_{eff} \frac{\partial k}{\partial x_j}) + G_k + G_b - \rho\varepsilon - Y_M \tag{4}$$

Equation for the energy dissipation (ε)

$$\frac{\partial}{\partial x_i}(\rho\varepsilon u_i) = \frac{\partial}{\partial x_j}(\alpha_\varepsilon \mu_{eff}\frac{\partial \varepsilon}{\partial x_j}) + G_k C_{1\varepsilon}\frac{\varepsilon}{k} - C_{2\varepsilon}\rho\frac{\varepsilon^2}{k} \quad (5)$$

Component transport equation

$$\nabla \cdot (\rho \vec{v} Y_i) = -\nabla \cdot \vec{J_\iota} + R_i + S_i \quad (6)$$

where τ_{ij} is the viscous shear stress ($\tau_{ij} = \mu\left(\frac{\partial u_i}{\partial x_j} + \frac{\partial u_j}{\partial x_i}\right)$), μ_{eff} is the effective kinematic viscosity ($\mu_{eff} = \mu + \mu_t$), G_k represents the generation of turbulence kinetic energy (can be defined as $G_k = -\rho\overline{u_i' u_j'}\frac{\partial u_j}{\partial x_i}$), α_k and α_ε are the turbulent Prandtl numbers for *k* and ε ($\alpha_k = \alpha_\varepsilon = 1.3$), $C_{1\varepsilon}$ and $C_{2\varepsilon}$ are two constants of the turbulent model ($C_{1\varepsilon} = 1.44$ and $C_{2\varepsilon} = 1.92$), $\vec{J_\iota}$ represents the diffusion flux of species ($\vec{J_\iota} = -\rho D_{i,m} + R_i$), R_i is the amount of component i produced or consumed in the reaction, S_i is the additional rate, and Y_M denotes the total dissipation rate due to the variable dilatation incompressible turbulence.

The Multiple Reference Frame (MRF) model is used to model the turbine region. It determines the velocity of the moving region by adding the rotation velocity on the original translational velocity. The velocity in the rotational region is given by:

$$\vec{v_r} = \vec{v} - \vec{\omega} \times \vec{r} \quad (7)$$

The governing equations of flow in the MRF model are modified as:

Continuity equation

$$\nabla \cdot (\rho\vec{v_r}) = 0 \quad (8)$$

Momentum equation

$$\nabla \cdot (\rho\vec{v_r}\vec{v_r}) + \rho(2\vec{\omega} \times \vec{v_r} + \vec{\omega} \times \vec{\omega} \times \vec{r}) + \rho\frac{\partial \vec{\omega}}{\partial t} \times \vec{r} = \nabla \cdot (\mu\nabla\vec{v_r}) + \mathrm{S}_{\vec{v_r}} \quad (9)$$

where $\vec{v}$ is the absolute velocity, $\vec{\omega}$ is the angular velocity vector, and $\vec{r}$ is the position vector.

The output power (P_t) can be computed as:

$$P_t = \frac{2\pi n M}{60} \quad (10)$$

where n is the rotation speed and M represents the total blade moments of the turbine.

The HPCR is simplified as a porous media. The governing equations of the HPCR region are expressed as:

Continuity equation:

$$\nabla \cdot (\gamma \rho \vec{v}) = 0 \tag{11}$$

Momentum equation:

$$\nabla \cdot (\gamma \rho \vec{v}) = -\gamma \nabla p(\gamma \vec{\tau}) + \gamma \rho \vec{g} + S_{\Phi} \tag{12}$$

where γ is the porosity, $\vec{\tau}$ is the viscous stress tensor, and S_{Φ} denotes the momentum loss term ($S_{\Phi} = -\left(\frac{\mu}{K}\vec{v} + \frac{C}{2}\rho|\vec{v}|\vec{v}\right)$).

The permeability (K) and inertia coefficient (C) are respectively defined in Equations (13) and (14) (Wang et al., 2014).

$$K = \frac{D_P^2}{150}\frac{\gamma^3}{(1-\gamma)^2} \tag{13}$$

$$C = \frac{3.5}{D_P^2}\frac{(1-\gamma)}{\gamma^3} \tag{14}$$

where D_P is the pore diameter.

The oxidation rate of CH_4 is given by (Haeger et al., 2004):

$$r_m = B \cdot \frac{B_1 c_1}{1+B_1 c_1}\frac{B_2 c_2}{1+B_2 c_2} \cdot SSA \tag{15}$$

where r_m is the reaction rate of CH_4 of the HPCR, c_1 and c_2 are respectively the concentrations of CH_4 and O_2, $B, B_1,$ and B_2 are respectively equal to 5.37×10^{-7}, 2.42, and 4.60, and SSA is the specific surface area of the HPCR ($SSA = \frac{6(1-\gamma)}{D_P}$) (Ming et al., 2021b).

The CH_4 removal performance of the SCPP-HPCR is evaluated by the photocatalytic efficiency (Equation (16)) and purification rate (Equation (17)) of CH_4.

$$\varepsilon_{methane} = \frac{J_1 - J_2}{J_1} \times 100\% \tag{16}$$

$$\dot{m}_{methane} = Q_m(m_1 - m_2) \tag{17}$$

where J_1 and J_2 are respectively the CH_4 concentrations at the inlet and outlet of the reactor, m_1 and m_2 are respectively the mass fractions of CH_4 at the entrance and exit, and Q_m is the mass flow rate of the SCPP-HPCR.

2.3 Boundary conditions

The SCPP-HPCR is powered by natural convection driven by the solar radiation. The boundary conditions for the collector inlet and chimney outlet are the pressure inlet and outlet, respectively. The collector surface is a convective heat transfer boundary,

and the coefficient is related to the ambient wind speed. The coefficient can be set to a constant value of 10 W/(m^2·K) while ignoring the ambient wind effect (Tingzhen et al., 2006). The surfaces of the chimney and turbine are adiabatic. The conversion of solar radiation to heat flux of the ground is an economical and effective method (Tingzhen et al., 2008). The conversion coefficient is related to the location of the area, air quality, and other factors. For example, the coefficient is 0.7 in a desert in northwest China, which indicates that the ground heat flux is almost 600 W/m^2, corresponding to a solar radiation of 857 W/m^2 (Ming et al., 2012). The details of the boundary conditions are presented in Table 1.

Table 1. Boundary conditions

Location	Type	Value
Inlet of SCPP-HPCR	Pressure inlet	p = 0 Pa, T = 293 K
Outlet of SCPP-HPCR	Pressure outlet	p = 0 Pa
Surface of ground	Heat flux	q = 200 - 600 W/m^2
Surface of canopy	Convection	T = 293 K, h = 10 W/(m^2·K)
Surface of chimney	Adiabatic	q = 0 W/m^2
Turbine	MRF	ω = 0 ~ 200 rpm
HPCR	Porous media	

2.4 *Grid system and numerical procedure*

The structured grid system has high better computational stability and shorter solution time. Structured grids are used for the whole computational domain, except the 3-D turbine, whose structure is complex. Moreover, the local grids of blade surface and HPCR region are densified to more correctly simulate the mass transfer process. The grid system as shown in Fig 2.

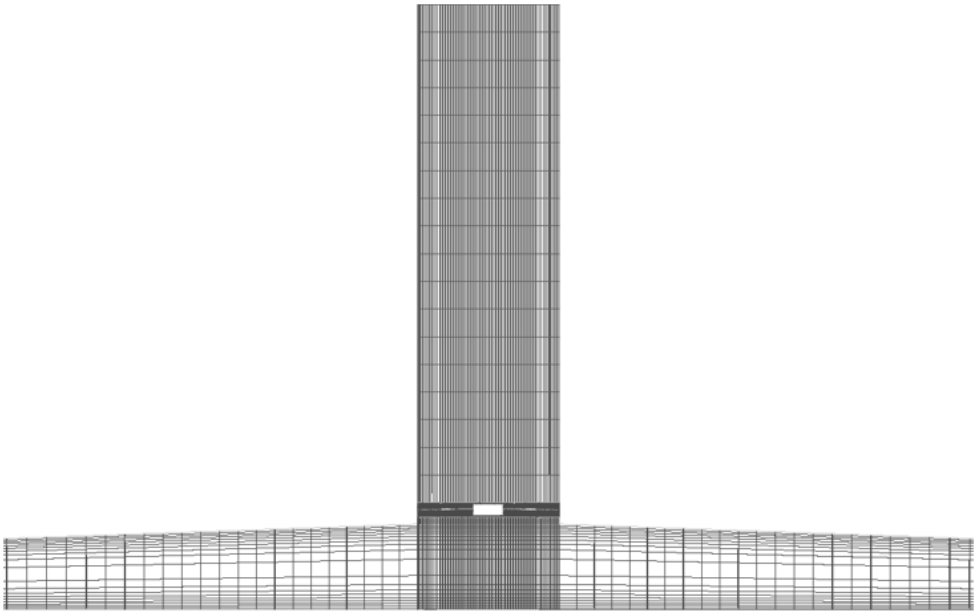

(a)

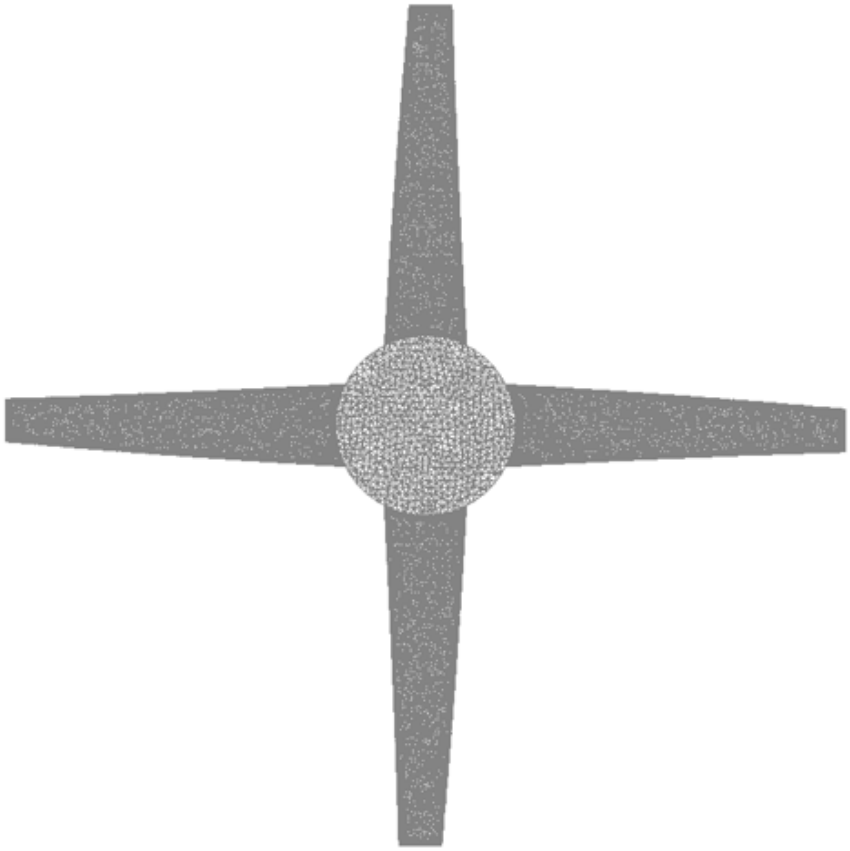

(b)

Fig 2 Grid system of the SCPP-HPCR: (a) Front view on the surface of Y = 0 m

and (b) grid distribution on the surface of the turbine.

The grid-independent is checked using three grid systems with grid numbers of 4,071,561, 3,112,516, and 2,316,115. The average velocities of the outlet are 8.61, 8.27, and 8.01 m/s, respectively, under G = 857 W/m^2 and ω = 100 rpm. The relative error of the simulation results between different grid systems is less than 3.94%. In this study, the grid system with the number of 3,112,516 is considered in the simulation.

The ANSYS FLUENT 19.0 software is used for the numerical simulation. The SIMPLE algorithm is used for the pressure–velocity coupling scheme. The PRESTO divergence scheme is used in the pressure term, and the upwind scheme is used in the other terms. The calculation results converged when the variations of the concentration of CH_4 and the velocity at the chimney outlet are less than 0.001, or the maximum residuals of all the equations are less than 10^{-5}.

2.5 Validation

The velocity of the chimney outlet and the photocatalytic efficiency of CH_4 are compared with the data presented in the reference (Ming et al., 2021b) to validate the numerical model at G = 857 W/m^2, ω = 0 rpm, and γ = 0.85. The obtained results are presented in Table 2. It can be seen that the velocity at the chimney outlet increased while the photocatalytic efficiency decreased with the increase of the pore diameter. The maximum relative error for the chimney outlet velocity is 8.55% when D_P = 2 mm, while the relative errors for other values of D_P are less than 4%. In fact, the study of (Ming et al., 2021b) did not build the 3-D turbine causing the grid discrepancy to be the primary reason for the error. In general, the results of the numerical simulations in this study are reasonable.

Table 2. Verification of the simulation results

Simulation results	Date form reference (Ming et al., 2021b)	Relative error (%)

Pore diameter (mm)	Velocity at outlet (m/s)	Photocatalytic efficiency of CH_4 (%)	Velocity at outlet (m/s)	Photocatalytic efficiency of CH_4 (%)	Velocity	Photocatalytic efficiency
2	8.42	96.32	7.70	96.02	8.55	0.31
2.5	8.56	93.56	8.27	92.42	3.39	1.22
3	8.71	89.40	8.56	88.38	1.72	1.14
3.5	9.02	84.97	8.81	84.12	2.33	0.99
4	9.29	80.47	8.92	80.11	3.98	0.44

3. Result and analysis

In this section, the influence of the pore size on the performance of the SCPP-HPCR is first discussed for γ = 0.85. The porosity of HRCR is then optimized to the equivalent CO_2 emission. Finally, the solar radiation data of Qianyanzhou, China, are considered as example to estimate the CO_2 emission reduction of the system for one day.

3.1 Analysis of flow field

Most of the solar energy is locked in the collector for air heating due to its one-way-screen property (Ming et al., 2017). The heated airflow could form a density difference with the ambient air, and be gradually collected at the bottom of the chimney to develop a strong upward airflow due to the buoyancy effect.

Fig. 3 shows the pressure distribution of the plane of Y = 0 m and Z = 1 m. There are two main contributors of resistance while the hot air flow is moving. Firstly, the porous structure can impede the passage of the airflow, generating a pressure gradient of roughly 93.3 Pa. Secondly, the airflow at the bottom of the chimney converts its own kinetic energy into mechanical energy, causing the turbine to rotate in to generate electricity. The maximum pressure differential is almost 942.7 Pa, with a significant positive pressure at the bottom and a negative pressure above the blade.

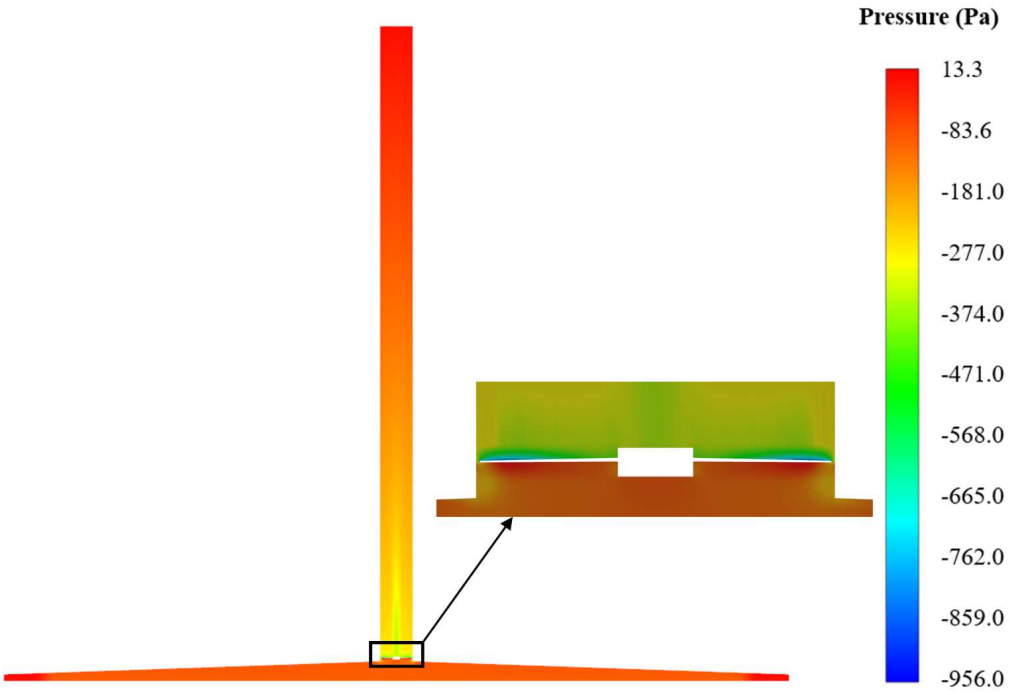

(a)

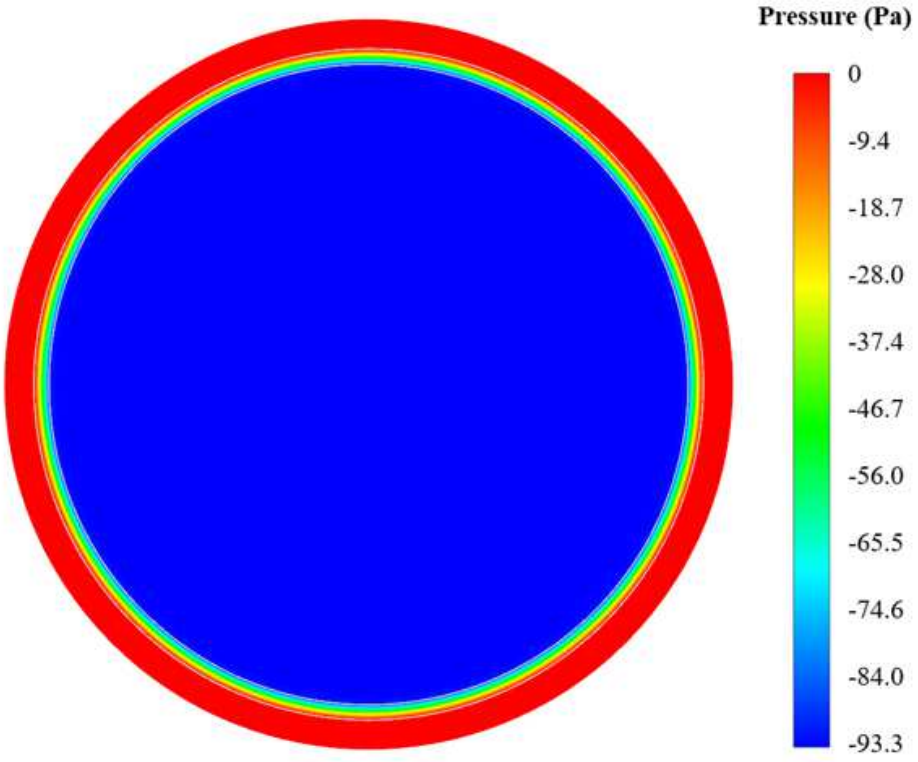

(b)

Fig. 3. Contours of the pressure distribution of the plane at G = 857 W/m^2, ω = 100 rpm, and D_P = 4 mm: (a) plane at Y = 0 m and (b) plane at Z = 1 m.

Fig. 4 shows the velocity distribution of the plane of Y = 0 m and Z = 1 m. The airflow enters at the entrance of the canopy and converges towards the center with increasing speed. The overall velocity is still modest (not exceeding 2 m/s), while the velocity at the edge of canopy is just 0.35 m/s, with a major increase only occurring near the chimney bottom. The airflow overcomes gravity and keeps going upward after passing through the turbine, and the velocity gradually decreases. However, the velocity of the air at the center of the wheel remains low.

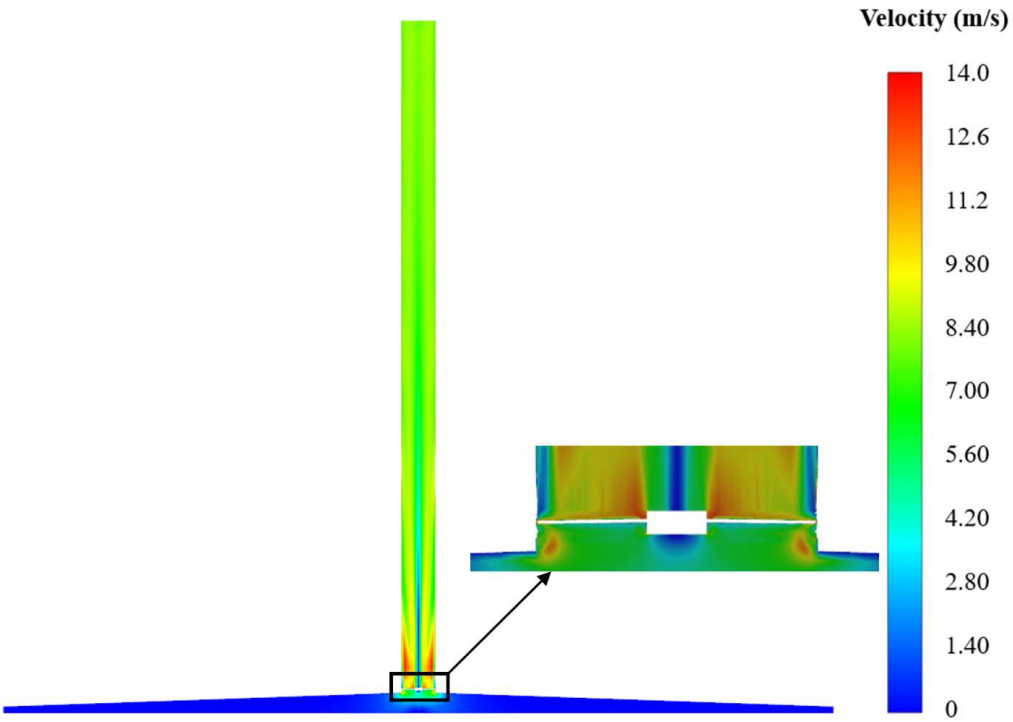

(a)

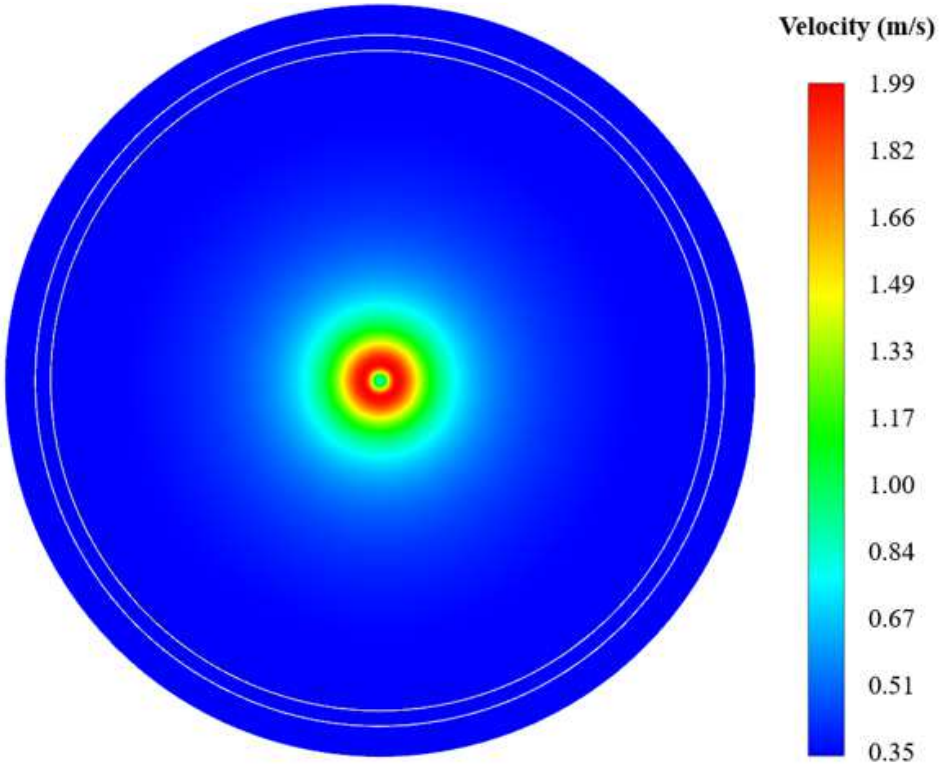

(b)

Fig. 4. Contours of the velocity distribution of the plane at G = 857 W/m^2, ω = 100 rpm, and D_P = 4 mm: (a) plane at Y = 0 m and (b) plane at Z = 1 m.

Fig. 5 shows the CH_4 distribution of the plane of Y = 0 m and Z = 1 m. The natural convection pulls CH_4 into the system at a concentration of 1.87 ppm from the atmosphere, where it is continually degrading in the HPCR along a distinct concentration gradient. The CH_4 degradation process is confined in, relative to the plate reactor (Ming et al., 2022; Xiong et al., 2022), and the distribution appears hierarchical. The CH_4 is evenly distributed and remained unchanged in the system after passing through the HPCR. For instance, the CH_4 concentration at the chimney outlet is 0.27 ppm and the photocatalytic efficiency is 85.56% at G = 857 W/m^2, ω = 100 rpm, and D_P = 4 mm.

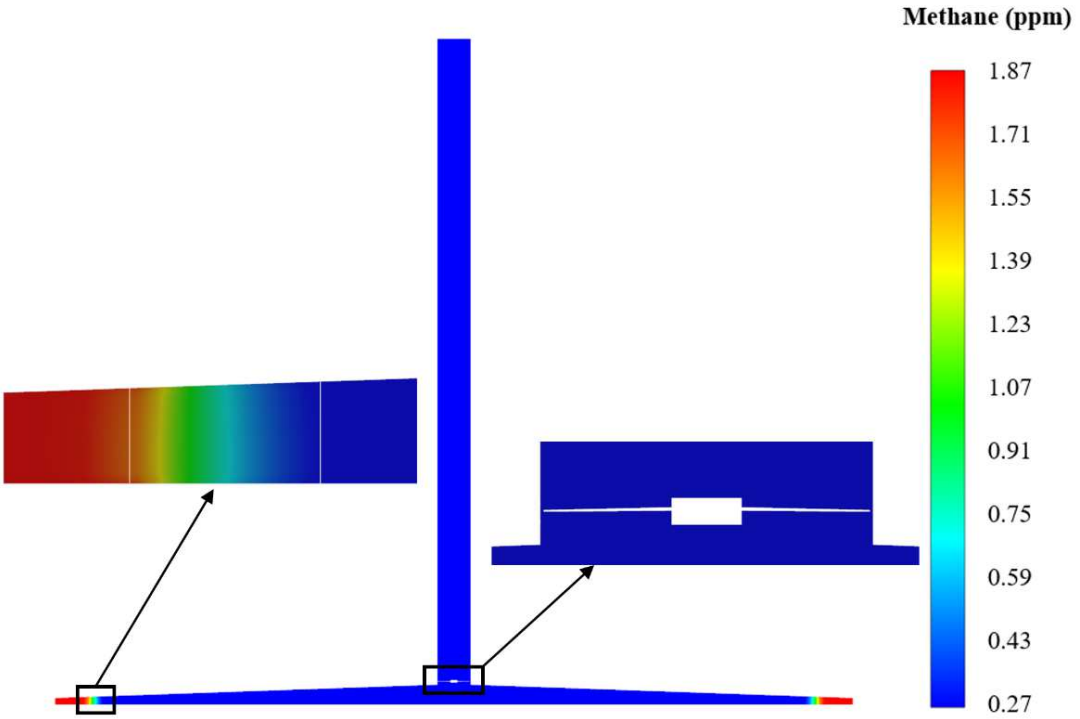

(a)

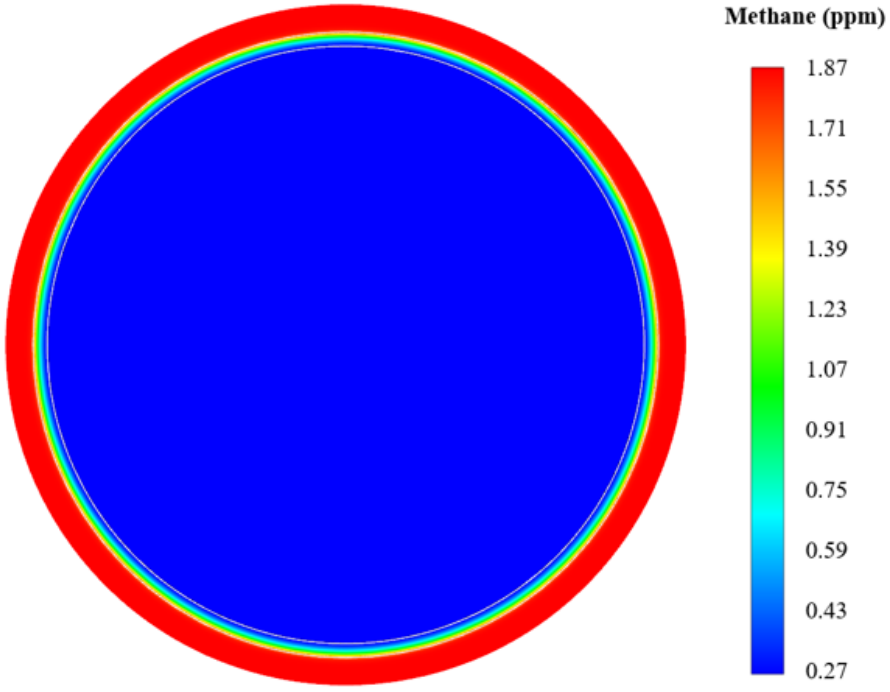

(b)

Fig. 5. Contours of the CH_4 distribution of the plane at G = 857 W/m^2, ω = 100 rpm, and D_P = 4 mm: (a) plane at Y = 0 m and (b) plane at Z = 1 m.

3.2 Performance analysis of SCPP-HPCR

Fig. 6 shows the average velocity at the chimney outlet. The airflow resistance through the turbine area increased as the turbine speed increased, so that more kinetic energy of the air is transformed into mechanical energy of the turbine. In addition, when the D_P of the honeycomb channel is small, the viscous resistance caused by the porous medium can dramatically increase, and the chimney exit velocity can decrease. According to the experimental data provided in Haff (Haaf, W., 1984), the exit velocity of the chimney was 9 m/s with G = 857 W/m^2 and ω = 100 rpm. The exit velocity loss is 8.2% when a reaction zone of D_P = 4 mm is within the canopy, while it is 15.7% for D_P = 2 mm.

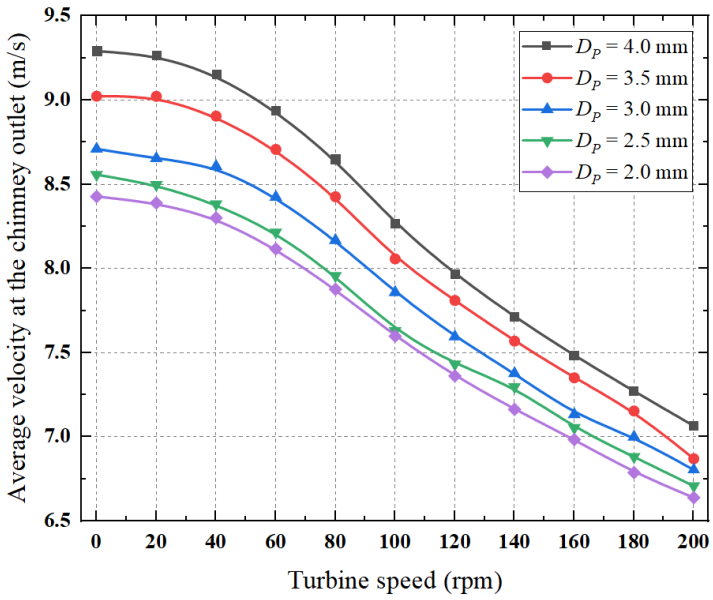

Fig. 6. Average velocity at the chimney outlet under different turbine speeds at G = 857 W/m^2.

The resistance of the turbine and reactor (Fig. 7), as well as the turbine speed, are the primary factors that affect the air flow inside the SCPP-HPCR. When the turbine speed increases, the pressure drop through the reaction zone constantly decreases, while the pressure drop through the turbine increases. An excessively high turbine speed can lower the mass flow rate of the system, obstruct airflow inside the canopy, and decrease the pressure loss caused by the HPCR. The latter is the primary source of internal

resistance when the turbine speed is low, but the turbine area is the primary source at high turbine speed. Furthermore, the overall pressure loss inside the system is first decreased and then increased. The overall internal pressure loss of the SCPP-HPCR is minimized to 176.84 Pa for G = 857 W/m^2, ω = 80 rpm, and D_P = 2 mm.

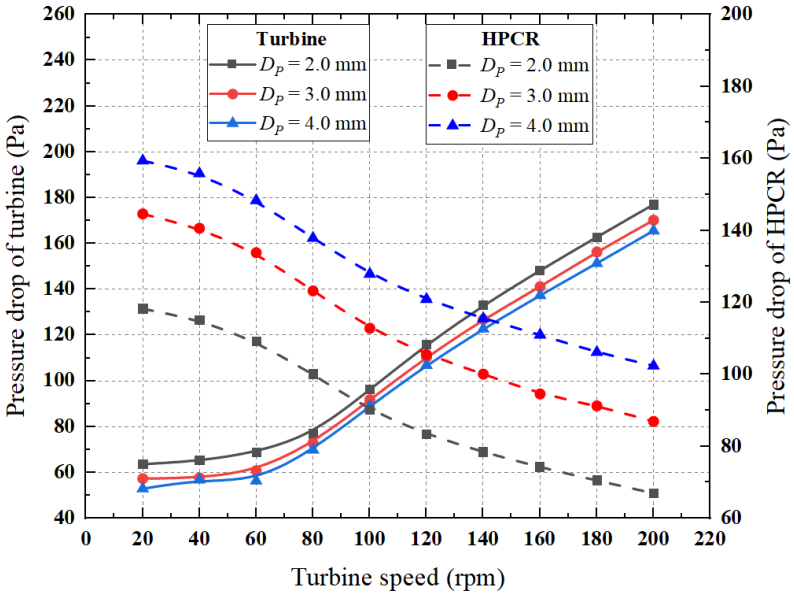

Fig. 7. Pressure drop of the turbine and HPCR under different turbine speeds at G = 857 W/m^2.

The two performance criteria of the SCPP-HPCR for removing atmospheric CH_4 are the photocatalytic efficiency and purification rate, as shown in Fig. 8. The former describes the level of CH_4 molecule purification, while the latter calculates the amount of CH_4 damaged by the system. The photocatalytic efficiency of CH_4 can be improved by increasing the turbine speed or reducing the reactor particle size. However, decreasing the mass flow rate of the system sharply reduces the purification rate. The photocatalytic performance of the system can be enhanced more by reducing the particle size in the honeycomb channel than by speeding up the turbine. For instance, the efficiency of the CH_4 photocatalytic is boosted by roughly 20% when the particle size is decreased from 4 mm to 2 mm, but only by 8% when the turbine speed is increased to 200 rpm. The impact of the turbine speed on the photocatalytic efficiency

becomes insignificant for $D_P \leq 3$ mm.

Increasing the turbine speed can only slightly lower the purge rate of CH_4, in the case where the turbine speed is low. A linear relationship between the turbine speed and the rate of purification can be observed when the turbine speed is high. The primary reason for the rate of purification decrease is the loss of mass flow rate brought by the increased turbine speed. The curves of the purification rate of CH_4 are pretty close for reactors having particle diameters of 2.5 mm, 3 mm, and 3.5 mm. Although the reactor with a smaller particle size seems more effective in lowering the atmospheric CH_4, the large pressure loss can undoubtedly have an adverse effect on the overall performance of the system. In addition, CH_4 generally has a high photocatalytic efficiency for D_P = 3 mm.

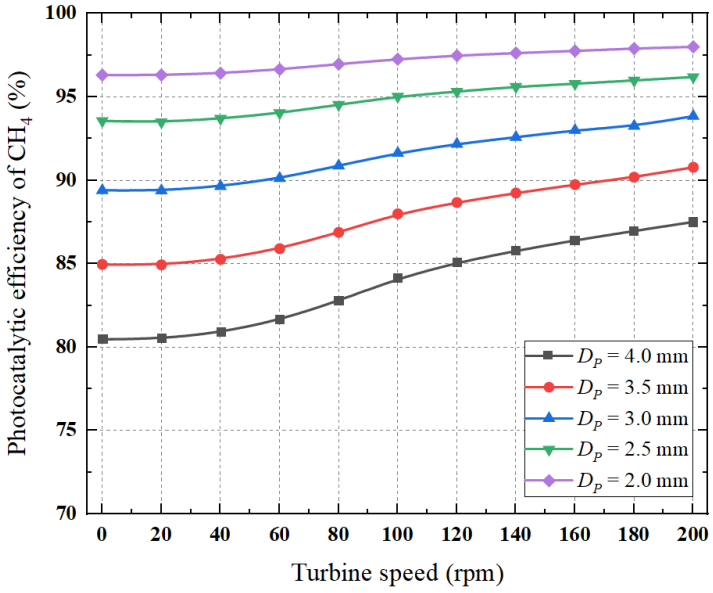

(a)

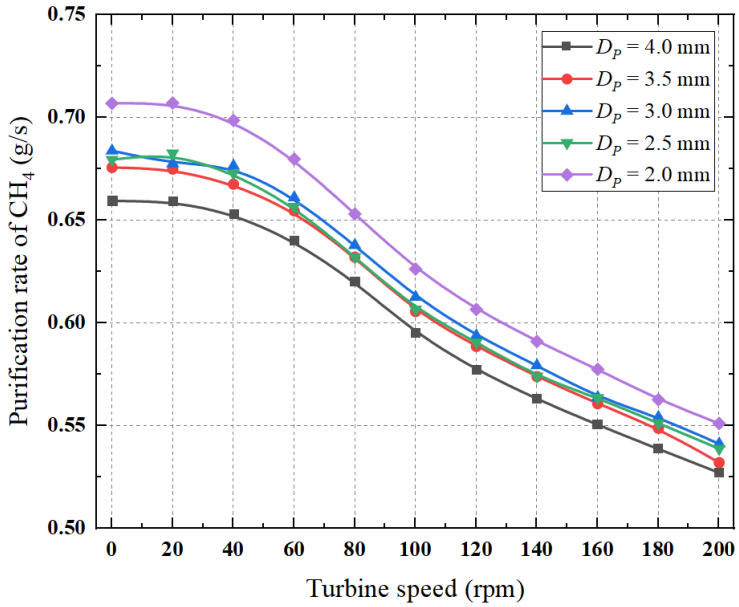

(b)

Fig. 8. Degradation of CH_4 under different turbine speeds at G = 857 W/m^2: (a) photocatalytic efficiency of CH_4 and (b) purification rate of CH_4.

The primary source of electricity for most countries is still the thermal power plants. Many pollutants are emitted during the burning of fossil fuels, such as CO_2, which is released on 0.95 kg for 1 kW of produced energy (Mittal et al., 2012). The SCPP can produce up to 36 kW of power and it is a zero-energy zero-pollution power source, which significantly reduces the CO_2 emissions from thermal power plants (Pasumarthi and Sherif, 1998).

The SCPP-HPCR is a CH_4 negative emission technology able to face the climate change using CO_2 equivalents. CH_4 had 84 times the GWP of CO_2 on a 20-year scale, which showed that reducing 1 kg of CH_4 is comparable to reducing 84 kg of CO_2 (Jackson et al., 2019). The CO_2 emission reduction rate of the SCPP-HPCR can be expressed as:

$$\dot{C_{eq}} = \dot{m}_{CH_4} \times 84 + \dot{m}1_{CO_2} - \dot{m}2_{CO_2} \quad (18)$$

where $\dot{m}_{CH_4}$ is the purification rate of CH_4, $\dot{m}1_{CO_2}$ is the reduction rate of CO_2 emission from coal-fired power station, and $\dot{m}2_{CO_2}$ is the generation rate of CO_2 from photocatalytic CH_4.

Fig. 9 shows the rate of CO_2 emission reduction of SCPP-HPCR. It can be seen that the rate of CO_2 emission reduction increases and then decreases at different reactor particle diameters. The emission reduction rate is nearly identical at lower turbine speeds, mostly because generating electricity from turbines at lower speeds results in less CO_2 reduction. The peak CO_2 reduction rate corresponds to a turbine speed between 160 rpm and 180 rpm for different particle sizes. In addition, the larger the particle size, the greater the reduction rate.

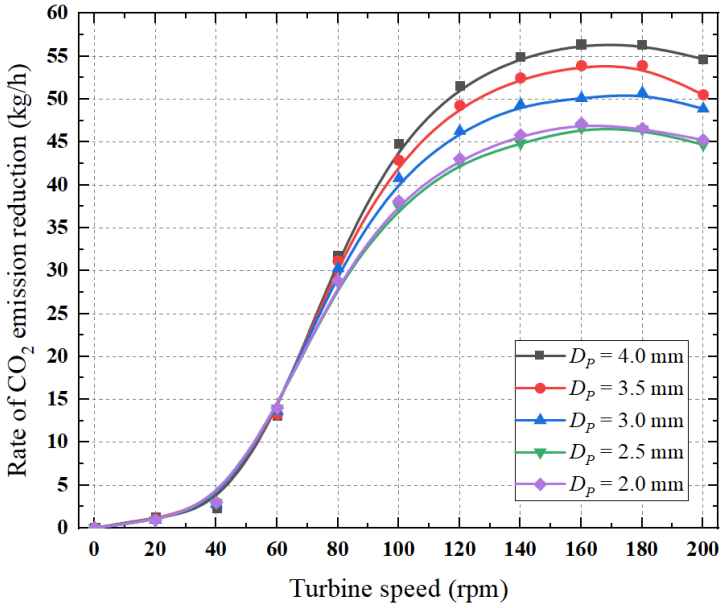

Fig. 9. Rate of CO_2 emission reduction under different turbine speeds at G = 857 W/m^2.

3.3 Optimization of the HPCR porosity

Porosity is another crucial factor that affected the overall performance of the SCPP-HPCR. The highest photocatalytic efficiency and purification rate are for D_P = 3 mm, as mentioned in section 3.2. Fig. 10 shows the CH_4 distribution in the HPCR at G = 857 W/m^2, ω = 180 rpm, and D_P = 3 mm. It is less difficult for atmospheric CH_4 to enter the HPCR as the porosity of the reactor increases because of the greater airflow resistance. The length of the concentration gradient of CH_4 in the reactor expands as the reactor's porosity, and the uniform concentration at the exit of the HPCR.

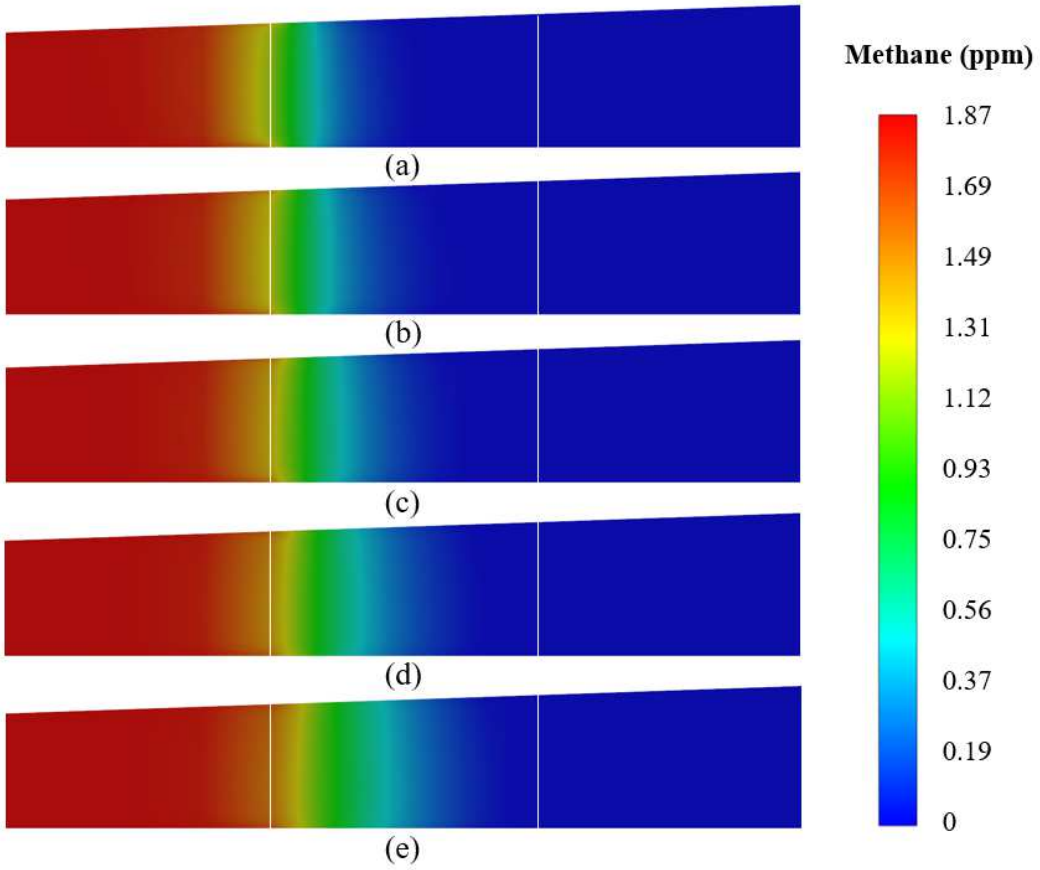

Fig. 10. Contours of the CH_4 distribution in the HPCR at G = 857 W/m^2, ω = 180 rpm, and D_P = 3 mm: (a) γ = 0.70, (b) γ = 0.75, (c) γ = 0.80, (d) γ = 0.85 and (e) γ = 0.90.

The impact of reactors with various porosities on the photocatalytic performance of the system is studied at D_P = 3 mm (Fig. 11). The HPCR with less porosity can have higher the SSA and longer times for CH_4 to contact with the photocatalyst when the particle diameter is kept constant. In addition, a decrease in porosity can make the porous media more viscous resistant, and impede the flow of gas. The purification rate peaks at a porosity of 0.85, while the photocatalytic efficiency decreases with the increase in the porosity. The CH_4 photocatalytic efficiency is 93.26% and the purification rate is 0.55 g/s at G = 857 W/m^2, D_P = 3 mm, and γ = 0.85.

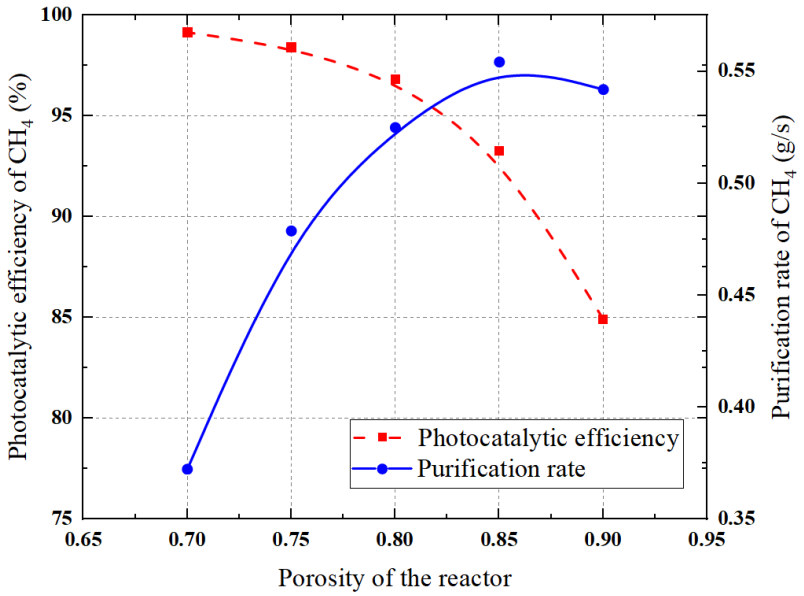

Fig. 11. Influence of the porosity on the CH_4 degradation performance of the SCPP-HPCR at G = 857 W/m^2.

3.4 Estimation of CO_2 emission reduction

Based on solar radiation data from July 24, 2016 (Ming et al., 2021b), the performance characteristics of the system for one day of operation were evaluated while assuming that an SCPP-HPCR will be built in Qianyanzhou, China. D_P = 3 mm, γ = 0.85, and a turbine at a constant speed of 180 rpm are chosen as the optimal parameters of the SCPP-HPCR. Ten groups of the solar radiation from 7:00 am to 5:00 pm are divided, and input parameters are established at one-hour intervals. The volumetric flow rate, turbulent pressure drop, output power, and CO_2 emission reduction of the system are presented in Table 3. The time-by-time photocatalytic performance curves of the system are shown in Fig. 12.

From 9:00 am until 3:00 pm, the solar radiation is high (more than 700 W/m^2). The solar radiation of a day first increased and then decreased. The rate of CO_2 reduction and the power generation of the turbine both peaks during this time period. The photocatalyst activity is fully stimulated due to the strong UV light in the environment, and the photocatalytic efficiency and rate of methane reaches their maximum values during this period. 375.52 kg of CO_2 and 2.38 kg of CH_4 can be mitigated by the system in one day of operation.

Table 3. Performance parameters of the SCPP-HPCR on July 24, 2016 in Qianyanzhou, China.

Time	Solar radiation (W/m^2)	Volume flow rate of the system (m^3/s)	Pressure drop of turbine (Pa)	Output power (kW)	CO_2 emission reduction (kg/h)
7:00-8:00	270	323.98	102.99	8.89	8.46
8:00-9:00	474	416.42	126.41	25.39	24.14
9:00-10:00	715.3	501.12	146.45	43.29	41.15
10:00-11:00	837.5	537.99	154.84	51.86	49.29
11:00-12:00	892.8	555.37	158.82	56.07	53.29
12:00-13:00	884.7	551.57	157.92	55.15	52.41
13:00-14:00	889.2	552.79	158.28	55.45	52.70
14:00-15:00	716.1	501.27	146.50	43.33	41.19
15:00-16:00	607.2	465.49	138.16	35.44	33.68
16:00-17:00	407.5	388.93	119.83	20.21	19.21

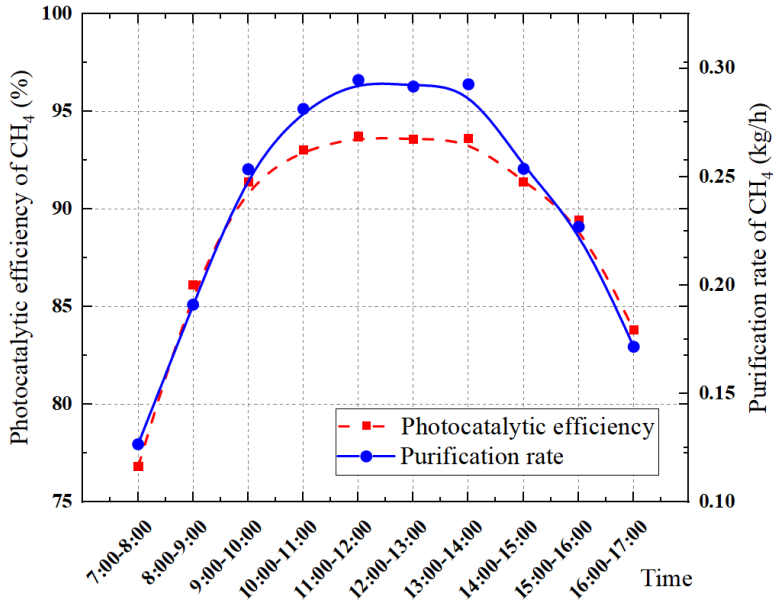

Fig. 12. Performance of CH_4 degradation on July 24, 2016 in Qianyanzhou, China.

As a massive energy storage layer, the soil can turn part of the solar energy into internal energy at day and release thermal energy at night to heat the air inside the collector, creating a steady thermal airflow and achieving all-weather intermittent power generation (Guo et al., 2016). The HPCR cannot perform well due to the lack of the UV light at night. The capacity of the system to reduce CO_2 can be further improved if an appropriate UV light source system is constructed around the HPCR (Wang et al., 2014).

4. Discussion

The high construction costs are still a concern to be considered even though SCPP-HPCR can remove atmospheric CH_4 while simultaneously producing electricity. The SCPP building cost is around $1.25 million in the desert, the Gobi, and other regions where lands are cheap (Abdelsalam et al., 2020). The original investment can be returned after 15 years of operation owing to the generating power of the system (Krätzig, 2013). SCPP is a long-term investment that will yield off with an expected lifespan of 80 years (Harte et al., 2013). It has the advantages of a simple structure and low maintenance. In comparison to other methods currently used to remove atmospheric CH_4, such as photocatalysis, thermal catalysis, electrocatalysis, etc., a large and continuous amount of energy must be consumed in to achieve the appropriate reaction conditions and provide steady airflow (Sher Shah et al., 2020). SCPP-HPCR forms a steady air stream to degrade atmospheric CH_4 by the HPCR and create economic value by the turbine power generation with no energy usage. In the future, highly selective photocatalysts can be used to remove other atmospheric pollutants.

5. Conclusion

As a novel negative emission technology, the SCPP-HPCR can effectively reduce the atmospheric CH_4 concentration, ultimately alleviating the global warming effect. In this paper, the CH_4 degradation and electricity generation performance of the SCPP-HPCR are studied based on a 3-D numerical model. The impact of the system on the environment is evaluated by the CO_2 equivalent. The following conclusions can be

drawn.

(1) The HPCR and the turbine area are the primary sources of internal resistance for low and high turbine speeds, respectively. The overall internal pressure loss of the SCPP-HPCR is minimized to 176.84 Pa for G = 857 W/m^2, ω = 80 rpm, and D_P = 2 mm.

(2) The photocatalytic efficiency of CH_4 can be enhanced by increasing the turbine speed or decreasing the D_P of the reactor. However, the latter can improve the efficiency more than the former.

(3) 375.52 kg of CO_2 and 2.38 kg of CH_4 can be mitigated by an SCPP-HPCP system built in Qianyanzhou, China, in one day for D_P = 3 mm, γ = 0.85, and ω = 180 rpm.

Acknowledgments

This research was supported by the National Key Research and Development Plan (Grant No. 2019YFE0197500), the European Commission H2020 Marie Curie Research and Innovation Staff Exchange (RISE) award (Grant No. 871998) , the National Natural Science Foundation of China (Grant No. 52278123), and the Fundamental Research Funds for the Central Universities (Grant No. 225206002).

References

Abdelsalam, E., Kafiah, F., Alkasrawi, M., Al-Hinti, I., Azzam, A., 2020. Economic Study of Solar Chimney Power-Water Distillation Plant (SCPWDP). Energies 13(11), 2789.

Ahmed, K., Wang, Y., Bai, Y., Sekar, K., Li, W., 2022. A carbon nanowire-promoted Cu2O/TiO2 nanocomposite for enhanced photoelectrochemical performance. New Journal of Chemistry 46(32), 15495-15503.

Allen, D., 2016. Attributing Atmospheric Methane to Anthropogenic Emission Sources. Acc Chem Res 49(7), 1344-1350.

Brenneis, R.J., Johnson, E.P., Shi, W., Plata, D.L., 2021. Atmospheric- and Low-Level Methane Abatement via an Earth-Abundant Catalyst. ACS Environmental Au 2(3), 223-231.

Bui, M., Adjiman, C.S., Bardow, A., Anthony, E.J., Boston, A., Brown, S., Fennell, P.S., Fuss, S., Galindo, A., Hackett, L.A., 2018. Carbon capture and storage (CCS): the way forward. Energy & Environmental Science 11(5), 1062-1176.

Cao, Q., Pui, D.Y., Lipinski, W., 2015. A concept of a novel solar-assisted large-scale cleaning system

(SALSCS) for urban air remediation. Aerosol and air quality research 15(1), 1-10.
Cao, Q.F., Kuehn, T.H., Shen, L., Chen, S.C., Zhang, N.N., Huang, Y., Cao, J.J., Pui, D.Y.H., 2018. Urban-scale SALSCS, Part I: Experimental Evaluation and Numerical Modeling of a Demonstration Unit. Aerosol Air Qual Res 18(11), 2865-2878.
Chen, X., Li, Y., Pan, X., Cortie, D., Huang, X., Yi, Z., 2016. Photocatalytic oxidation of methane over silver decorated zinc oxide nanocatalysts. Nature communications 7(1), 1-8.
de Richter, R., Ming, T.Z., Davies, P., Liu, W., Caillol, S., 2017. Removal of non-CO2 greenhouse gases by large-scale atmospheric solar photocatalysis. Prog Energ Combust 60, 68-96.
Fuss, S., Lamb, W.F., Callaghan, M.W., Hilaire, J., Creutzig, F., Amann, T., Beringer, T., de Oliveira Garcia, W., Hartmann, J., Khanna, T.J.E.R.L., 2018. Negative emissions—Part 2: Costs, potentials and side effects. 13(6), 063002.
Galpern, D.M., 2021. A View from Glasgow. Sustainability and Climate Change 14(6), 360-365.
Guo, P., Li, J., Wang, Y., 2014. Numerical simulations of solar chimney power plant with radiation model. Renewable Energy 62, 24-30.
Guo, P.H., Li, J.Y., Wang, Y.F., Wang, Y., 2016. Evaluation of the optimal turbine pressure drop ratio for a solar chimney power plant. Energ Convers Manage 108, 14-22.
Haaf, W., 1984. Solar chimneys: part ii: preliminary test results from the Manzanares pilot plant. International Journal of Sustainable Energy 2(2), 141-161.
Haaf, W., 1984. Solar tower, part ii: Preliminary test results from the manzanares pilot plant. Solar Energy 2, 41-61.
Haeger, A., Kleinschmidt, O., Hesse, D., 2004. Kinetics of photocatalyzed gas reactions using titanium dioxide as the catalyst Part II: Photocatalyzed total oxidation of alkanes with oxygen. Chem Eng Technol 27(9), 1019-1026.
Harte, R., Höffer, R., Krätzig, W.B., Mark, P., Niemann, H.-J., 2013. Solar updraft power plants: Engineering structures for sustainable energy generation. Engineering Structures 56, 1698-1706.
House, K.Z., Baclig, A.C., Ranjan, M., van Nierop, E.A., Wilcox, J., Herzog, H.J., 2011. Economic and energetic analysis of capturing CO2 from ambient air. Proc Natl Acad Sci U S A 108(51), 20428-20433.
Jackson, R.B., Solomon, E.I., Canadell, J.G., Cargnello, M., Field, C.B., 2019. Methane removal and atmospheric restoration. Nat Sustain 2(6), 436-438.
Krätzig, W.B., 2013. Physics, computer simulation and optimization of thermo-fluidmechanical processes of solar updraft power plants. Sol Energy 98, 2-11.
Kuylenstierna, J.C., Michalopoulou, E., Malley, C., 2021. Global Methane Assessment: Benefits and costs of mitigating methane emissions.
Li, Y., Li, J., Zhang, G., Wang, K., Wu, X.J.A.S.C., Engineering, 2019. Selective photocatalytic oxidation of low concentration methane over graphitic carbon nitride-decorated tungsten bronze cesium. 7(4), 4382-4389.
Li, Z., Pan, X., Yi, Z.J.J.o.M.C.A., 2019. Photocatalytic oxidation of methane over CuO-decorated ZnO nanocatalysts. 7(2), 469-475.
Ma, H.K., Yang, H.A., 2010. A Comparative Study of TiO2 Nanoparticles Synthesized in Premixed and Diffusion Flames. Journal of Thermal Science 19(6), 567-575.
Maia, C.B., Silva, J.D.C., 2022. Thermodynamic assessment of a small-scale solar chimney. Renewable Energy 186, 35-50.
Masson-Delmotte, V., Zhai, P., Pirani, A., Connors, S.L., Péan, C., Berger, S., Caud, N., Chen, Y., Goldfarb, L., Gomis, M., 2021. Climate change 2021: the physical science basis. Contribution of working

group I to the sixth assessment report of the intergovernmental panel on climate change, v-vii.
Ming, T.Z., de Richter, R., Oeste, F.D., Tulip, R., Caillol, S., 2021a. A nature-based negative emissions technology able to remove atmospheric methane and other greenhouse gases. Atmos Pollut Res 12(5), 101035.
Ming, T.Z., Gui, H.Y., Shi, T.H., Xiong, H.B., Wu, Y.J., Shao, Y.M., Li, W., Lu, X.H., de Richter, R., 2021b. Solar chimney power plant integrated with a photocatalytic reactor to remove atmospheric methane: A numerical analysis. Sol Energy 226, 101-111.
Ming, T.Z., Wang, X.J., de Richter, R.K., Liu, W., Wu, T.H., Pan, Y., 2012. Numerical analysis on the influence of ambient crosswind on the performance of solar updraft power plant system. Renew Sust Energ Rev 16(8), 5567-5583.
Ming, T.Z., Wu, Y.J., de Richter, R.K., Liu, W., Sherif, S.A., 2017. Solar updraft power plant system: A brief review and a case study on a new system with radial partition walls in its collector. Renew Sust Energ Rev 69, 472-487.
Ming, T.Z., Xiong, H.B., Shi, T.H., Wu, Y.J., Wang, C.X., Wen, Y.G., Li, W., de Richter, R., Zhou, N., 2022. A novel green technology: Reducing carbon dioxide and eliminating methane from the atmosphere. International Journal of Energy Research 46(14), 20107-20120.
Minx, J.C., Lamb, W.F., Callaghan, M.W., Fuss, S., Hilaire, J., Creutzig, F., Amann, T., Beringer, T., de Oliveira Garcia, W., Hartmann, J.J.E.R.L., 2018. Negative emissions—Part 1: Research landscape and synthesis. 13(6), 063001.
Mittal, M.L., Sharma, C., Singh, R., 2012. Estimates of emissions from coal fired thermal power plants in India, 2012 International emission inventory conference. pp. 13-16.
Pastohr, H., Kornadt, O., Gürlebeck, K., 2004. Numerical and analytical calculations of the temperature and flow field in the upwind power plant. International Journal of Energy Research 28(6), 495-510.
Pasumarthi, N., Sherif, S., 1998. Experimental and theoretical performance of a demonstration solar chimney model—Part I: mathematical model development. International Journal of Energy Research 22(3), 277-288.
Price, S.J., Sherlock, R.R., Kelliher, F.M., McSeveny, T.M., Tate, K.R., Condron, L.M., 2004. Pristine New Zealand forest soil is a strong methane sink. Global Change Biol 10(1), 16-26.
Sanchez, D.L., Johnson, N., McCoy, S.T., Turner, P.A., Mach, K.J., 2018. Near-term deployment of carbon capture and sequestration from biorefineries in the United States. Proc Natl Acad Sci U S A 115(19), 4875-4880.
Sekar, K., Chuaicham, C., Vellaichamy, B., Li, W., Zhuang, W., Lu, X., Ohtani, B., Sasaki, K., 2021. Cubic Cu2O nanoparticles decorated on TiO2 nanofiber heterostructure as an excellent synergistic photocatalyst for H2 production and sulfamethoxazole degradation. Applied Catalysis B: Environmental 294, 120221.
Sher Shah, M.S.A., Oh, C., Park, H., Hwang, Y.J., Ma, M., Park, J.H., 2020. Catalytic Oxidation of Methane to Oxygenated Products: Recent Advancements and Prospects for Electrocatalytic and Photocatalytic Conversion at Low Temperatures. Adv Sci (Weinh) 7(23), 2001946.
Tingzhen, M., Wei, L., Guoliang, X., 2006. Analytical and numerical investigation of the solar chimney power plant systems. International Journal of Energy Research 30(11), 861-873.
Tingzhen, M., Wei, L., Guoling, X., Yanbin, X., Xuhu, G., Yuan, P., 2008. Numerical simulation of the solar chimney power plant systems coupled with turbine. Renewable Energy 33(5), 897-905.
Vazquez-Ruiz, A., Navarro, J.M.A., Hinojosa, J.F., Xamán, J.P., 2022. Computational Fluid Dynamics and Experimental Analysis of the Heat Transfer in a Room With a Roof Solar Chimney. Journal of

Thermal Science and Engineering Applications 14(4), 1-26.
Vellinga, P., Swart, R., 1991. The greenhouse marathon: A proposal for a global strategy. Climatic Change 18(1), vii-xii.
Wang, Q., Xiong, H., Ming, T., 2022. Methods of Large-Scale Capture and Removal of Atmospheric Greenhouse Gases. Energies, p. 6560.
Wang, X., Tan, X., Yu, T., 2014. Modeling of Formaldehyde Photocatalytic Degradation in a Honeycomb Monolith Reactor Using Computational Fluid Dynamics. Industrial & Engineering Chemistry Research 53(48), 18402-18410.
Wang, Y., Ming, T., Li, W., Yuan, Q., de Richter, R., Davies, P., Caillol, S.J.G.G.S., Technology, Atmospheric Removal of Methane by enhancing the natural hydroxyl radical sink.
Witze, A., 2019. Dramatic sea-ice melt caps tough Arctic summer. Nature 573(7774), 320-322.
Xiong, H., Ming, T., Wu, Y., Wang, C., Chen, Q., Li, W., Mu, L., de Richter, R., Yuan, Y., 2022. Numerical analysis of solar chimney power plant integrated with CH4 photocatalytic reactors for fighting global warming under ambient crosswind. Renewable Energy 201, 678-690.
Zhang, J., Wang, Y., Wang, Y., Bai, Y., Feng, X., Zhu, J., Lu, X., Mu, L., Ming, T., de Richter, R., Li, W., 2022. Solar Driven Gas Phase Advanced Oxidation Processes for Methane Removal - Challenges and Perspectives. Chemistry, e202201984.
Zuo, L., Liu, Z.H., Dai, P.Z., Qu, N., Ding, L., Zheng, Y., Ge, Y.T., 2021. Economic performance evaluation of the wind supercharging solar chimney power plant combining desalination and waste heat after parameter optimization. Energy 227, 120496.
Zuo, L., Liu, Z.H., Ding, L., Qu, N., Dai, P.Z., Xu, B.F., Yuan, Y., 2020. Performance analysis of a wind supercharging solar chimney power plant combined with thermal plant for power and freshwater generation. Energ Convers Manage 204, 112282.
Zuo, L., Yan, Z., Zhou, T., Liu, S., Zheng, Y., Ge, Y., 2022. Study on the Influence of Windproof Cylinder on the Performance of Solar Vortex Power-desalination Integrated System, 2022 IEEE 5th International Electrical and Energy Conference (CIEEC). IEEE, pp. 1821-1825.